Research Paper

Rigorous light-scattering simulations of nanophase iron space-weathering effects on reflectance spectra of olivine grains

Antti Penttilä [a,*], Timo Väisänen [a], Johannes Markkanen [b], Julia Martikainen [a], Tomáš Kohout [c], Gorden Videen [d], Karri Muinonen [a,e]

[a] Department of Physics, University of Helsinki, P.O. box 64, FI-00014, Finland
[b] Max Planck Institute for Solar System Research, Justus-von-Liebig-Weg 3, D-37077, Göttingen, Germany
[c] Department of Geosciences and Geography, University of Helsinki, P.O. box 64, FI-00014, Finland
[d] Space Science Institute, Boulder, CO 80301, USA
[e] Geospatial Research Institute FGI, National Land Survey, Geodeetinrinne 2, FI-02430 Masala, Finland

ARTICLE INFO

ABSTRACT

We present a multi-scale light-scattering model that is capable of simulating the reflectance spectra of a regolith layer. In particular, the model can be applied to a case where the regolith grains have varying amounts of nanophase inclusions due to space weathering of the material. As different simulation tools are employed for different size scales of the target geometry (roughly, nano-, micro-, and millimeter scales), the particle size effects, the surface reflections, and the volume scattering can all be properly accounted for. Our results with olivine grains and nanophase iron inclusions verify the role of the nanoinclusions in the reflectance spectra of space-weathered materials. Together with the simulation results, we give simplified explanations for the space-weathering effects based on light scattering, namely the decrease of albedo, the general increase of the red spectral slope, and the dampening of the spectral bands. We also consider the so-called ultraviolet bluing effect, and show how the change in the spectral slope over the ultraviolet–visual wavelengths is due to the decrease of reflectance in the visual wavelengths rather than the increase of reflectance in the ultraviolet part.

1. Introduction

Space weathering refers to processes that alter the surfaces of atmosphereless solar system bodies. These processes have been studied in experiments, and many of the material changes are understood (e.g., Keller and McKay, 1997; Sasaki et al., 2002, 2003; Chapman, 2004; Brunetto et al., 2006; Noguchi et al., 2011; Kohout et al., 2014; Matsuoka et al., 2015; Pieters and Noble, 2016; Gillis-Davis et al., 2017). The material changes are thought to cause changes in the reflectance spectra of space-weathered objects via light-scattering mechanisms. The spectral changes include the darkening of the reflectance spectra, as well as the changes in the slope of the spectra and in the depths of the spectral attenuation bands.

We are inspired by the experimental work by Noble et al. (2007) on space weathering, followed by the work by Lucey and Riner (2011), who proposed an improvement on the Hapke model (Hapke, 2001) to explain the experiments. These works revealed the need to update the Hapke model to take into account the size of the inclusions generated by space weathering in the host regolith grains in order to properly explain the space-weathering effects in the ultraviolet–visual–near-infrared (UV–vis–NIR) spectral range. More recently, there have been continued attempts to include more detail in the optical modeling of space weathering (Moroz et al., 2014; Escobar-Cerezo et al., 2018; Jiang et al., 2019).

While the replacement of the Maxwell–Garnett effective-medium approximation (EMA) with the exact Mie theory by Lucey and Riner (2011) seems to fix the inclusion size effects in the Hapke model, we want to go further in the field of light-scattering modeling of regolith surfaces and introduce a multi-scale light-scattering model that offers a more fundamental approach. In detail, our approach is based on exact Maxwell-equation solvers, the geometrical optics approximation, and the radiative-transfer (RT) solution, all linked together as a multi-scale modeling pipeline. Our goal is not only to model, but to understand the relevant mechanisms in light scattering that cause the well-known spectral effects of space weathering (see Fig. 1 and, e.g., Chapman, 2004; Pieters and Noble, 2016). As this work is the first publication introducing our multi-scale model with space weathering, we keep the application simple and concentrate only on olivine as the regolith material, and nanophase iron ($npFe^0$) as the space-weathering product.

---

* Corresponding author.
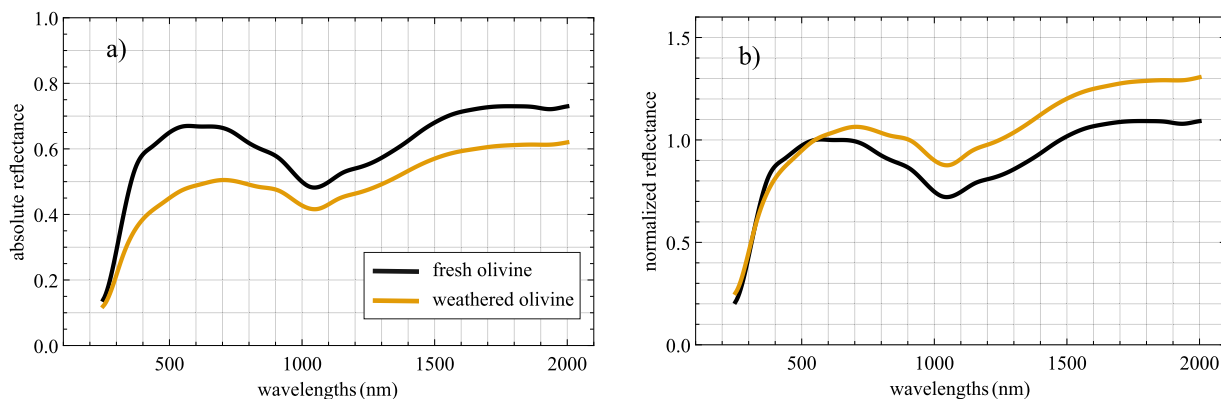 *E-mail address:* antti.i.penttila@helsinki.fi (A. Penttilä).

Fig. 1. The absolute (a) and the normalized (b, at 550 nm) spectra of fresh, non-weathered olivine, and olivine after a space-weathering-simulating thermal treatment (Forsterite content 93%, see (Kohout et al., 2014)). The measurements are made with the University of Helsinki spectrometer (Penttilä et al., 2018). The sample is illuminated at an angle of 10°, and the hemispherical reflectance is measured using an integrating sphere. The measured signal is divided with the calibration signal from a white Teflon sample with known properties. After calibration, the values are fractions of reflectance to a perfect Lambertian surface, i.e., 'absolute reflectance'. We can see the main effects of the space-weathering process in the spectra: (i) the general darkening, (ii) the dampening of the spectral absorption bands, and (iii) the slope of the spectra becoming more positive, i.e., slope reddening.

In Section 2, we introduce and explain our light-scattering modeling pipeline. In Section 3, we show the results of the modeling, and examine some space-weathering spectral effects. Finally, in Section 4, we discuss the potential applications of our modeling approach to space-weathering studies.

2. Methods

We present a new methodology for the computational modeling of the space-weathering effects on reflectance spectra. The methodology consists of a multi-scale light-scattering model with three individual codes for the three size scales (i.e., roughly nano-, micro-, and millimeter scales), together with a shape model for the olivine grains, and optical constant models for the materials olivine and nanophase iron. In the following, we give a detailed presentation of these methods.

2.1. Optical constants

The optical constants of the materials are crucial input parameters in the light-scattering model, and they will have a dominant effect on the output of the simulation over the other physical properties, such as the shape and the size of the particles. The optical constants are actually functions of the wavelength, and can be expressed with the complex refractive index $m(\lambda) = n(\lambda) + i\,k(\lambda)$, where n and k are the real and imaginary parts of the refractive index. Both are functions of the wavelength λ.

For nanophase iron, we employ the latest measurements by Cahill et al. (2019). They measured the complex refractive index of iron unexposed to ambient atmosphere for the wavelengths of 160–3590 nm. For olivine, we use the optical constants data for the Stubachtal olivine from the Jena database[1], which is for the wavelengths 200–2000 nm.

As the npFe^0 inclusions are in the olivine grain matrix, we require the relative refractive index of nanophase iron in olivine, m_{rFe}, to be used in the light-scattering computations regarding the properties of a single nanophase inclusion particle (see Section 2.3). The relative refractive index is given by $m_{\mathrm{rFe}} = m_{\mathrm{Fe}}/m_{\mathrm{ol}}$, where m_{Fe} is the complex refractive index of nanophase iron, and m_{ol} that of olivine. In Fig. 2, we show the optical constant models for nanophase iron, olivine, and nanophase iron in olivine, which are used in the present work.

2.2. Geometrical model for the material

In our three-stage light-scattering simulation, we model a plane-parallel, optically semi-infinite slab of regolith consisting of individual olivine grains. We model the npFe^0 inclusions as located in a shallow rim on the olivine grain surface (Keller and McKay, 1997). Starting from the smallest size scale, we model the npFe^0 inclusions as having spherical shapes. Their sizes should be some tens of nanometers at maximum, if we refer to laboratory measurements (e.g., Keller and McKay, 1997; Sasaki et al., 2002, 2003; Noble et al., 2007; Noguchi et al., 2011; Kohout et al., 2014; Pieters and Noble, 2016). On the other hand, there are reports of larger iron or iron sulfate inclusions after space weathering, called micro- or Britt–Pieters particles (Pieters and Noble, 2016). To study the effect of the size, we mainly use 20-nm (in diameter) inclusions, but also test 100-nm and 200-nm inclusions.

The 20-nm inclusions are small compared to the visible and NIR wavelengths. Their size parameter $x = 2\pi r/\lambda$, where r is the radius of the particle, is between 0.0314 and 0.314 for $\lambda = 2000$ nm and $\lambda = 200$ nm, respectively. These size parameters reside in or near the Rayleigh-scattering regime.

The single olivine grains in the regolith layer are of a larger size scale and we use the Gaussian random sphere model for their shape (Muinonen et al., 1996, 2009). We choose the parameters of the Gaussian sphere so that the relative standard deviation of the radius is 10%, and the power-law index of the angular correlation function is -2 (see Eq. (28) in Muinonen et al. (2009) for details). When modeling the space-weathered grains, the npFe^0 inclusions are randomly located in a 200-nm thick mantle layer of the grains. An example of the geometry is shown in Fig. 3. The mantle layer actually consists of amorphous host matrix (see, e.g., Keller and McKay, 1997), but the change in optical constants between the amorphous rim and the host olivine is not known to us. Therefore, we will treat the mantle as regular olivine in this study. In any case, the amorphous rim should be spectrally featureless, so large effects from this simplification are not foreseen.

Finally, the single olivine grains are packed within a semi-infinitive planar layer having infinite vertical range and infinite depth. As we compute the vector radiative-transfer solution to this semi-infinite planar layer with the single olivine grains as diffuse scatterers, we are assuming that the particles are well separated and thus in the far-field of each other. In this case, the packing density or the mean-free-path length properties in the layer have no effect on the result.

2.3. Nanometer-scale scattering

The npFe^0 inclusions are in the size scale of some nanometers to some tens of nanometers, although larger iron or iron sulfate grains, the
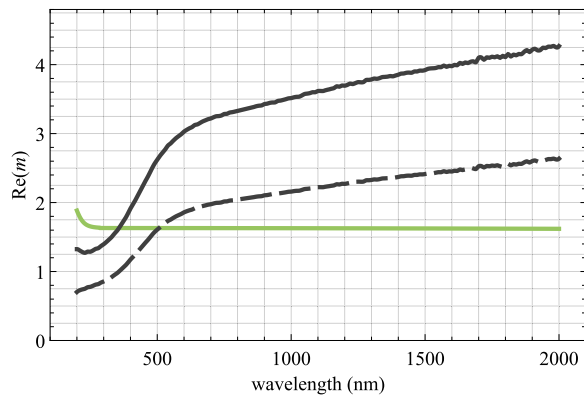

Fig. 2. The optical constants m_{ol}, m_{Fe}, and m_{rFe}, as a function of wavelength in the relevant range.
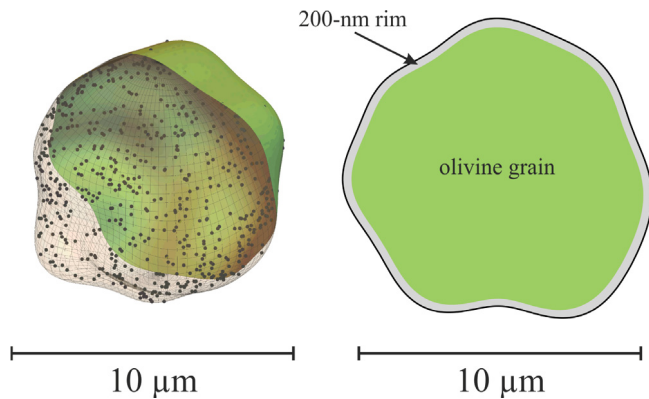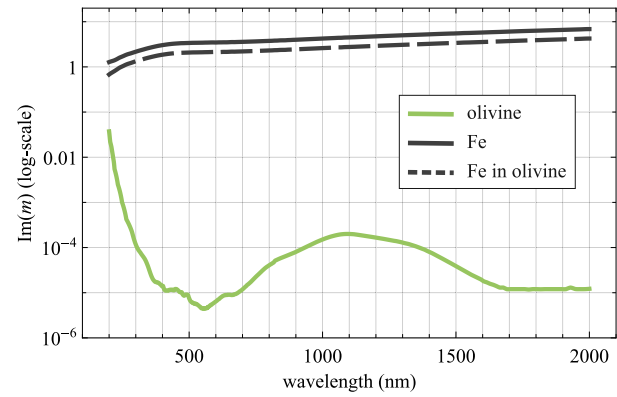

Fig. 3. An example of the Gaussian random sphere shape for the olivine grains. On the left, a 3D image with the grain, where the surface has been removed from the foremost half to show the npFe^0 inclusions below the surface. On the right, a 2D section of the particle showing the 200-nm rim, where the npFe^0 inclusions are located.

Fig. 4. The absorption and scattering efficiencies Q_{abs} and Q_{sca} for 20-nm npFe^0 inclusions in the olivine matrix using the Mie theory.

Britt–Pieters grains starting from some hundreds of nanometers to micrometers in size, are also reported (Lucey and Riner, 2011; Pieters and Noble, 2016). Regarding the light-scattering models, the size parameter x (i.e., size compared to the wavelength, see Section 2.2) is dictating the needs for the modeling. When $x \ll 1$, the Rayleigh approximation is accurate enough to describe the scattering and absorption. However, when x starts to approach one, exact methods such as the Mie scattering are needed to accurately describe the scattering properties of particles. Also, with size parameters close to and over one, the shape of the particle starts to influence its scattering properties more strongly. Therefore, for non-spherical particles with $x > 1$, a method other than Mie but based on the exact solution for the Maxwell equations is needed. These include, for example, the surface- and volume-integral-methods (see, e.g., Mishchenko et al., 2000).

In this study, the space-weathering products are generally small ($x < 1$), but we want to test also the effect of larger inclusions. Based on microscope imaging of space-weathered materials (e.g., Noble and Pieters, 2003; Noble et al., 2005; Noguchi et al., 2011; Pieters and Noble, 2016) the shape of the inclusions is quite spherical, and the inclusions do not seem very elongated. The Mie scattering approach is accurate enough for 20-nm npFe^0 grains even if not exactly spherical because their size relative to the wavelength is small, and the use of a general volume-integral-equation method or similar would complicate the simulations significantly. We also tested if the inclusions should have a size distribution, but again, due to their small size parameter, it did not make a difference. Thus, we choose to model the shape of the inclusions, also when testing some larger ones, with spherical shape and the Mie scattering model.
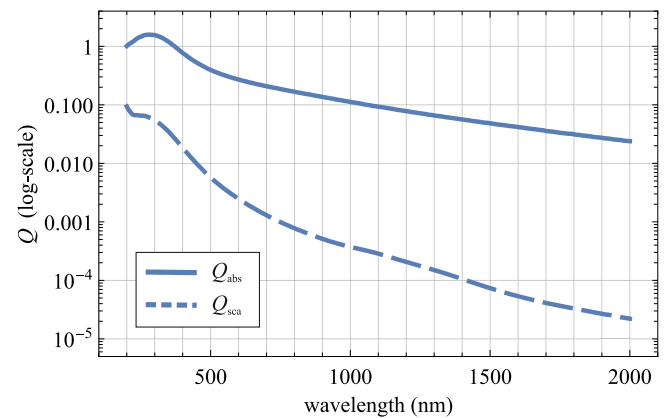
For the next size scale in our scattering model, we need the scattering properties of the npFe^0 inclusions (embedded in olivine matrix) as the input. Namely, we need the full Mueller matrix (Brown, 2014a) of the inclusions, as a function of the scattering angle, and the absorption and scattering cross sections of the particle. The Mueller matrix will give us the directional scattering information of the inclusions, needed in the vector RT simulations, while the cross sections are needed to compute the single-scattering albedo and the mean-free path parameters. For small particles, the scattering phase functions (the $(1,1)$ element in the 4×4 Mueller matrix) are quite similar for all the size parameters. A more interesting behavior is seen in the absorption and scattering efficiencies Q_{abs} and Q_{sca}, which are the corresponding optical cross sections divided by the geometrical cross section. In Fig. 4, we show the absorption and scattering efficiency for 20-nm npFe^0 inclusions in the olivine matrix. The relative optical constants for the nanophase iron come from the models described in Section 2.1.

One can see from Fig. 4 that the absorption is the main effect with the npFe^0 inclusions, being still one magnitude larger than the scattering with the shortest wavelengths around 200 nm. We can note that the Rayleigh approximation would actually produce the cross sections practically identical to the Mie results with the 20-nm inclusions (results not shown here), but this would not be true for larger sizes or size parameters. The Rayleigh approximations for the scattering and absorption efficiencies are

$$Q_{sca} = \frac{8}{3} x^4 \left| \frac{(m/m_0)^2 - 1}{(m/m_0)^2 + 2} \right|^2 \quad \text{and}$$

$$Q_{abs} = 4 x \, \mathrm{Im} \left(\frac{(m/m_0)^2 - 1}{(m/m_0)^2 + 2} \right), \tag{1}$$

with m as the refractive index of the material, and m_0 as the refractive index of the host matrix (van de Hulst, 1957).

The dominance of the absorption over scattering together with the small volume densities of the npFe^0 considered here (see Section 3) are the reasons why we can rely on the classical vector RT approach when including the nanophase inclusions as diffuse scatterers in the next simulation step (see Section 2.4). Some recent studies show that a volume element containing several scatterers with exactly modeled incoherent multiple-scattering properties would be the proper way to model dense-media radiative transfer (Muinonen et al., 2018; Markkanen et al., 2018; Väisänen et al., 2019).

2.4. Micrometer-scale scattering

The second size scale in the model is the scale of a single olivine regolith grain. Although the size distribution of the regolith can be quite wide, starting from some nanometer-sized dust and ending at centimeter- or even meter-sized boulders, the effective size (average size weighted with the particle cross-sectional area) should be in the scale of one/ten/hundred micrometers (Deb, 2015). The exact light-scattering methods become currently computationally too demanding for size parameters about and over one hundred, which corresponds to about 6.4 μm to 64 μm in diameter with wavelengths from 200 nm to 2000 nm. The light scattering from particles larger than that can be computed with quite good accuracy by combining geometric optics treatment (i.e., reflections and refractions from surfaces, absorption along the path) with diffuse scattering from small inclusions, as is done in the SIRIS code (Muinonen et al., 2009). The latest version of the code[2] can deal with core–mantle geometries, and therefore with cases where the npFe^0 inclusions are located in a thin mantle layer of the grain (Lindqvist et al., 2018; Martikainen et al., 2018).

The code is used to compute both the scattering properties (i.e., the Mueller matrix, the absorption and scattering cross sections) of non-weathered and weathered regolith grains. The size of the grain and the optical constants information about the material of the grain are given as input to the code. With weathered grains, also the scattering properties of the npFe^0 inclusions are needed.

2.5. Millimeter-scale scattering

In the final size scale, a macroscopic planar layer consisting of fresh or space-weathered olivine grains is considered. The layer is semi-infinite in depth and in horizontal directions, so all the incident radiation is either reflected backwards from the layer, or absorbed into the layer. The output of the vector RT solution is the bidirectional reflectance distribution function (BRDF) of a planar element, and the total hemispherical reflectance. The final size scale can present any 'macroscopic' planar element where there is a multitude of single regolith grains, so from millimeters to any size where the layer would still be planar. The total hemispherical reflectance is a function of the incident angle, integrated over the upper (backward scattered) hemisphere of the planar layer. In this work, we consider only incident light from the normal direction of the surface.

For the vector RT solution, we employ the so-called Radiative Transfer with Coherent Backscattering (RT-CB)[3] code, which is a Monte Carlo particle RT solver (Muinonen, 2004). Including the coherent backscattering (CB) effects in the code would require providing the amplitude scattering matrix for the scatterers (i.e., olivine grains), but the previous step with the SIRIS geometrical optics code can produce only the Mueller matrices, so the CB contribution to RT is omitted. However, the CB would affect only in the small angular lobe around the

---

[2] SIRIS4.2 with inhomogeneous waves in absorbing media and core–mantle geometry available from http://wiki.helsinki.fi/display/PSR/.

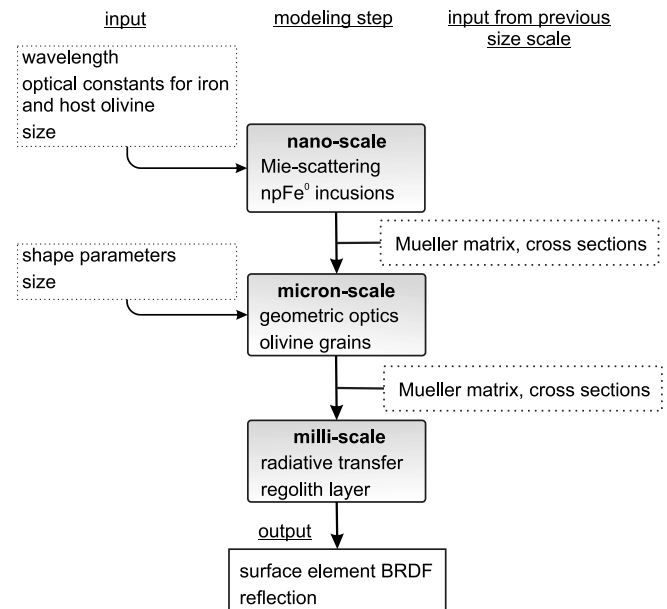[3] RT-CB code available from http://wiki.helsinki.fi/display/PSR.

Fig. 5. A schematic chart showing the flow of input parameters and intermediate results between the three codes for the different size scales.

light source direction, so we conclude that the difference compared to the RT-only solution in the total hemispherical reflectance is negligible.

This final scale completes our multi-scale simulation method. The computational flow is schematically described in Fig. 5. Since the optical properties of olivine and nanophase iron change with the wavelength, the simulation needs to be executed separately for each wavelength.

3. Results and discussion

We employ our models for the optical constants (Section 2.1) and run our multi-scale light scattering model Sections (2.3–2.5) for a range of wavelengths from 200 nm to 2000 nm. In this section, we will review the results and their implications on the light-scattering explanation of the space-weathering effects.

3.1. Regolith grain size

Although the regolith grain size is not a space-weathering effect, our simulations can also help to assess the effective grain size in the regolith. In Fig. 6, we show how the effect of small absorption in the single regolith grain multiplies when dealing with a layer of those single scatterers. We also show the grain-size effects on the resulting reflectance.

In Fig. 6, there are 10-, 20-, and 40-μm (in diameter) monodispersed, fresh (i.e., non-space-weathered) grains used in the simulation. The overall reflectance is decreasing with the increasing size of a single grain. This is due to the different ratio between the surface area and the volume of the grains. The absorption is effective in the volume, so the larger grains with smaller relative surface area will have smaller reflectance. The smaller grains have relatively more surface scattering and more multiple scattering, and therefore also larger reflectance.

If we compare either the absolute or the relative band depths between the local maximum reflectance around 550 nm and the local minimum reflectance around 1050 nm for both the measurements (see Fig. 1) and the simulations (Fig. 6), we can see that the 10-μm grains give the band depth from 550 nm to 1050 nm that is closest to the measurements. The absolute reflectance level of the real, measured olivine is somewhat lower than with the simulated one, probably due to some impurities and surface roughness in the real sample.
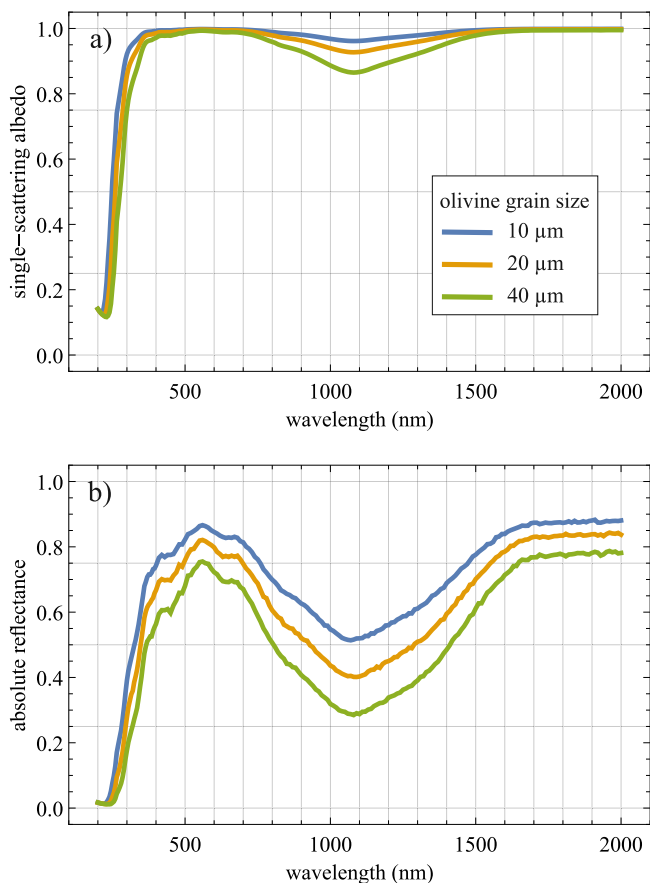
Fig. 6. In the plot (a), the single-scattering albedo of individual fresh olivine grains is plotted as a function of the wavelength. This is the result from the second, micrometer-scale step in our simulation chain. In the plot (b), the simulation from (a) is continued with the final, millimeter-scale simulation step, and the reflectance of the planar layer consisting of these grains is shown.

Since the olivine grains with size of 10 μm produce the most realistic results regarding the band depth, we will choose to use that size in the following simulations in this study.

3.2. Nanophase iron inclusion sizes

From our simulations, we can see the different effects on the spectra that are caused by the small inclusions (a few tens of nanometers at most) and the large inclusions (some hundreds of nanometers and more). In the literature, it is speculated that the small sizes both darken and redden the spectra, as the larger ones only darken (Pieters and Noble, 2016). We confirm this effect. The reddening effect of the small inclusions is coming from their Rayleigh-like absorption behavior that can be seen in Fig. 7. With the smallest wavelengths, the size parameter for the small inclusions is close to one, so close to the so-called resonance area, where both the scattering and absorption efficiencies are large. For the relative optical constants of nanophase iron in olivine, the absorption is the governing effect from these two. As the wavelength is increasing, the size parameter is decreasing together with the absorption efficiency (see Eq. (1)).

With the larger inclusions, the size/wavelength effect described above is only starting to have effect with the larger wavelengths. For example, with the 100-nm inclusions, the absorption starts to decrease only after about the 1000-nm wavelength, and with the 200-nm inclusions, the wavelength is around 1500 nm, as seen in Fig. 7. Furthermore, with the small inclusions, the scattering is at least one

magnitude smaller than the absorption. With larger sizes, the scattering remains at approximately the same level with the absorption up to wavelengths of about 1000 nm (100-nm inclusions) or 1500 nm (200-nm inclusions). In an earlier computer simulation experiment by Martikainen et al. (2018), it was shown that the larger (micrometer-scale) iron particles can be used to generally darken the spectra in olivine–pyroxene mixtures.

In Fig. 8, we show how the difference in the inclusion absorption behavior shows up in the final modeling results with the planar layer reflectance. The small npFe^0 inclusions are introducing both reddening and darkening in the spectra, while the larger inclusions only introduce a constant darkening before their reddening effect starts to play a role at about 1500-nm wavelength. We also tested other 'small' sizes for the npFe^0 inclusions (results not shown here), and noticed that the exact size in the range of roughly 5–30 nm does not have a large effect on the shape of the reflectance as a function of the wavelength, as shown in Fig. 8 for the 20-nm inclusions.

In the results presented below, we will focus on the small 20-nm npFe^0 inclusions. It can be mentioned, that we also tested the Maxwell–Garnett effective-medium approximation (EMA) as

$$m_{\mathrm{eff}}^2 = m_{\mathrm{ol}}^2 \left(1 - \frac{3(m_{\mathrm{ol}}^2 - m_{\mathrm{Fe}}^2)v}{2m_{\mathrm{ol}}^2 + m_{\mathrm{Fe}}^2 + (m_{\mathrm{ol}}^2 - m_{\mathrm{Fe}}^2)v} \right) , \qquad (2)$$

where v is the volume fraction of nanophase iron in the olivine grain (Liu et al., 2014). We then compared a case where the 20-nm npFe^0 inclusions were located in the 200-nm mantle layer in the 10-μm olivine grain to a case (*i*) where the effective optical properties of the 10-μm grain with npFe^0 inclusions were estimated with the EMA, and to a case (*ii*) where the effective optical properties of the 200-nm mantle only were estimated with the EMA. In the case (*i*), the inclusions are thought to be distributed uniformly throughout the grain. In the case (*ii*), the grain is thought to have a core and a 200-nm mantle with different optical properties.

Interestingly, for a 0.1% volume fraction of npFe^0 in the mantle, the EMA results (*i*) with the uniformly distributed nanophase iron material in the grain showed almost identical spectral reflectance with our multi-scale light-scattering model results (results not shown here). However, the case (*ii*) with the EMA-modeled mantle layer differed slightly from the other two results. We conclude that the EMA approach would be sufficient with very small inclusions (size parameter ≪ 1) and with very small amounts. The 0.1% volume fraction in the 200-nm mantle of a 10-μm grain corresponds to ∼ 0.01 % fraction in the whole volume, and with this fraction the EMA seems to work well. However, with the more realistic case with the EMA-modeled material only within the thin mantle with 0.1% volume fraction, the results are not performing that well when compared to our exact Mie simulations. Also, since there is no dependence on the inclusion size in EMA, it cannot be used to study the size effects.

3.3. Decreasing albedo

The explanation to the decreasing overall reflectance (i.e., albedo) is quite straightforward. We showed in Fig. 4 how the absorption governs the behavior of the 20-nm npFe^0 inclusions in the olivine matrix, being one-to-three magnitudes larger than the scattering. So, the small npFe^0 inclusions always increase the ability of the regolith to absorb light. Our main result is shown in Fig. 9, and one can see how the absolute reflectance is decreased with increasing amount of npFe^0 with all the wavelengths from 200 nm to 2000 nm.

3.4. Dampening of the absorption bands

As space weathering proceeds, the overall albedo is decreasing, but it has been seen that the absorption band depths also decrease. We claim that this behavior can be easily explained with simple scattering
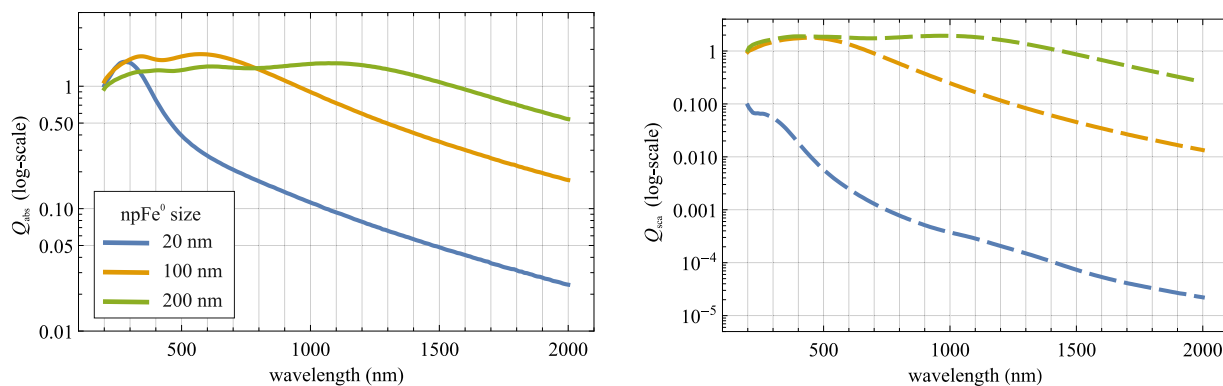
Fig. 7. The efficiencies for absorption (Q_{abs}, in the left) and scattering (Q_{sca}, in the right) for the 20, 100, and 200-nm nanophase iron inclusions in an olivine matrix, as a function of wavelength. Please note that the efficiency scale in the left goes down to 10^{-2}, but down to 10^{-5} in the right.
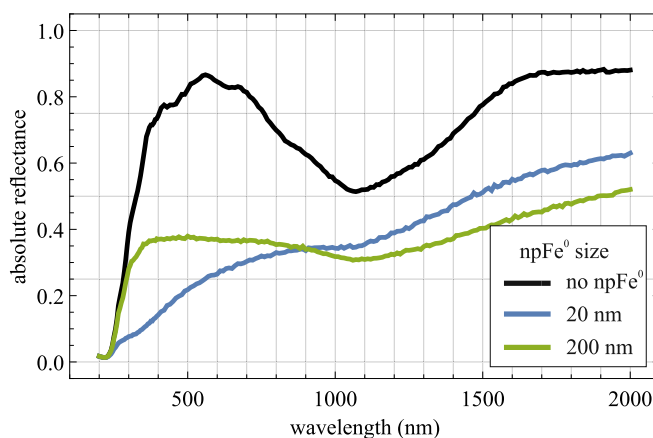

Fig. 8. The reflectance of a planar surface element consisting of fresh or weathered olivine grains. The nanophase iron inclusions have been either 20 or 200 nm in size, and their volume fraction in the surface rim was 0.1%.

approximations. First of all, we already showed that the effective-medium approximation can be valid for small inclusions and small fractions (Section 3.2). If we study how the Maxwell–Garnett EMA is behaving when modeling the imaginary part of the effective refractive index k_{eff}, we can notice that when a transparent host material (olivine) is combined with very absorbing inclusions (nanophase iron), there is a quite constant increase in the imaginary part of the effective refractive index. For example, if for simplicity we would fix the real parts of the refractive indices of olivine and nanophase iron to $n_{\mathrm{ol}} = 1.63$ and $n_{\mathrm{Fe}} = 3.4$, and the imaginary parts at 700 nm and at 1100 nm to $k_{\mathrm{ol}}\,(700\,\mathrm{nm}) = 1.0 \times 10^{-5}$, $k_{\mathrm{ol}}\,(1100\,\mathrm{nm}) = 2.0 \times 10^{-4}$, $k_{\mathrm{Fe}}\,(700\,\mathrm{nm}) = 3.6$, and $k_{\mathrm{Fe}}\,(1100\,\mathrm{nm}) = 4.5$. Then, the imaginary part of the effective refractive index according to the EMA with a 0.1% volume fraction of inclusions would be $k_{\mathrm{eff}}\,(700\,\mathrm{nm}) = 7.9 \times 10^{-4}$ and $k_{\mathrm{eff}}\,(1100\,\mathrm{nm}) = 8.3 \times 10^{-4}$. So, when moving from the fresh material to the weathered material, the 20-times difference in the extinction between the 700-nm and 1100-nm wavelengths for fresh olivine has decreased to 1.05-times increase for the space-weathered olivine.

The explanation for the dampening of the absorption bands can be continued with the Beer–Lambert type (i.e., $\exp(-\kappa\,l)$, where l is the path length in the material) reflectance. The Beer–Lambert reflectance as a function of the extinction coefficient κ can be very nonlinear. Especially, constant increases for an initially smaller κ will have a significantly larger change in the reflectance compared to the same increase for an initially larger κ. We verify the absorption band dampening in our simulation results, shown in Fig. 9.

3.5. Local slopes

All the local slopes in the reflectance spectra are also affected by the general dampening of the absorption bands mentioned above. An initial local slope can be blue/negative when going from high reflectance to the absorption band, or red/positive when going from the band to high reflectance. Either way, the nonlinear effect of space weathering on the absolute reflectance guarantee that the blue slopes will get less blue, and the red slopes will get less red, so there is a tendency towards a locally flat spectrum.

3.6. Spectral reddening

While the local slopes are decreasing, there is a general reddening seen in the reflectance spectra of space-weathered materials. We already saw in Section 3.2 that this can be related with the presence of small, less than some tens of nanometers, nanophase iron inclusions in the host grain. We can model the realistic case with the inclusions located in a shallow mantle layer in the grain. Fig. 7 shows why spectral reddening is not happening for inclusions larger than about 100 nanometers, at least not in the vis–NIR wavelength range — the Rayleigh-like $1/\lambda$ decrease in absorption starts to be effective only after $\lambda = 1000$ nm for the larger particles, and the absorption is still one magnitude larger than with the 20-nm grains at $\lambda = 2000$ nm. In Fig. 8 we show how the results change when the Mie results for the inclusions are further processed with the micro- and millimeter scale models to produce the surface element reflectance.
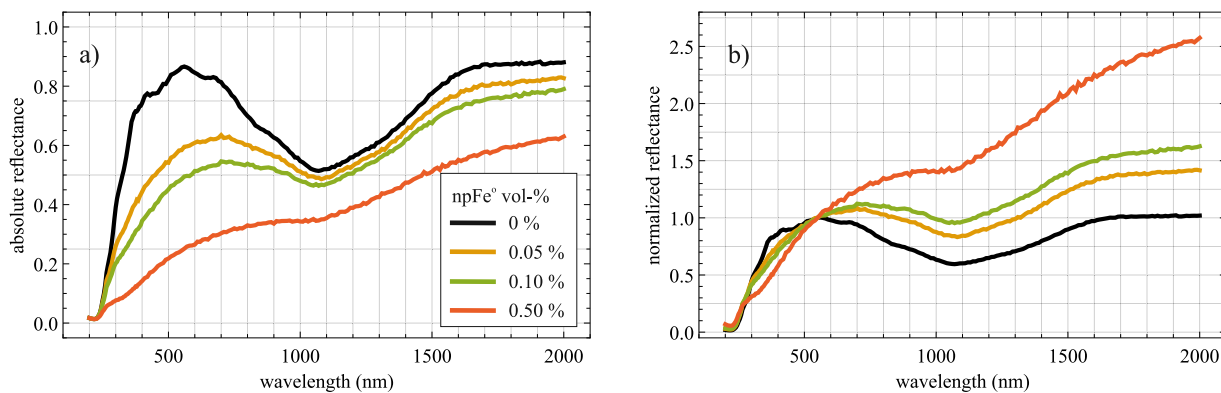
Fig. 9. Simulated effects of space weathering on spectra. (a) The absolute reflectance of an olivine regolith surface element as a function of the wavelength for both the 10 μm fresh olivine grains and the grains with varying amount of 20-nm npFe^0 inclusions. (b) The same but the reflectance is normalized at 550 nm. The volume fractions 0.05%, 0.1%, and 0.5% refer to volume fractions in the 200-nm thin mantle layer in the grains.

We can also test how the amount of the npFe^0 inclusions is affecting the reflectance spectra. In Fig. 9, we take the 10-μm grains and start to increase the fraction of the npFe^0 in the surface mantle. We go from fresh (i.e., 0% of npFe^0) material to volume fractions of 0.05%, 0.1%, and 0.5% in the mantle.

For the simulations, it is possible to define the volume fractions in the mantle. However, in experimental measurements one would probably see mass fractions of nanophase iron in the whole olivine grain. By assuming a density of 3.32 g/cm^3 for olivine and 7.874 g/cm^3 for nanophase iron, the mantle volume fractions would correspond to 0.013%, 0.026%, and 0.13% in mass for the whole grain.

3.7. UV bluing

For UV and visual wavelengths, there has been studies of the so-called UV bluing effect (see, e.g., Hendrix and Vilas, 2006; Vilas and Hendrix, 2015). To our understanding, the term *UV bluing* should refer to the change in the red spectral *slope* to less red (i.e., bluing) when measured over the UV–visual wavelength range. Our results are confirming this trend and are showing this change in the slope in the UV–visual range, see Fig. 9. In fact, we see the same decrease of all local slopes with space weathering, as was described in Section 3.5. However, we feel that the UV bluing is sometimes interpreted as there would be an increase of the regolith reflectance in the UV (see, e.g., Vilas et al., 2015). We would like to point out that, according to our results, with the refractive indices used in this work (Section 2.1) starting from the wavelength of 200 nm, we see no evidence of absolute increase of brightness with space weathering, not at UV wavelengths nor at any other wavelengths in our study.

The absorption coefficient of olivine increases rapidly when moving from visual to UV, resulting in a rapid decrease in reflectance. However, the Fe absorption coefficient is still larger, so the fresh olivine reflectance continues to be larger than that of the space-weathered olivine in the absolute scale. Even with wavelengths approaching 200 nm, where the scattering efficiency of the npFe^0 is increasing, the absorption efficiency of the inclusions is still one magnitude larger (see Fig. 4).

The difference between the fresh and the space-weathered olivine is largest close to the wavelength of 550 nm, where the fresh olivine is bright, due to the nonlinear effect of darkening by space weathering (see Section 3.4). On the other hand, spectra are often presented not in an absolute scale but in a normalized scale, and often normalized at 550 nm. The normalization shifts the absolute differences at 550 nm towards the UV and NIR in the normalized spectra. We claim that this procedure can perhaps give the impression that with UV bluing, the effect is caused by an increase of reflectance that is taking place at UV wavelengths. However, the UV bluing (when strictly meaning the

decrease of the red *slope*) with space weathering is a consequence of the rapid reflectance decrease at the visual wavelengths around 550 nm, according to our results (Fig. 9).

One recent study on the 'spectral bluing' is the paper by Brown (2014b) presenting simulations regarding the single-scattering albedo increase of individual particles. He studied a wide range of size parameters, and concluded that close to the size parameter scale $x \in [0.5, 1.2]$ the spectral bluing is the strongest (Brown, 2014b). While we agree with his method and conclusions, we would like to point out that the nanophase inclusions probably have size smaller than $x = 0.5$. For example, the 20-nm inclusions have $x = 0.31$ with $\lambda = 200$ nm, and the size parameter will be decreasing from that value as $1/\lambda$ with increasing wavelength. The scattering explanation in Brown (2014b) could be relevant for npFe^0 when the wavelength is smaller than 200 nm as the size parameter of the inclusions would approach the suitable range, but not for wavelengths above 200 nm.

4. Conclusions

We have presented a multi-scale light-scattering simulation method that can be used to study the effect of small inclusions in the grains of granular, packed material. In particular, this method is suitable of simulating space weathering effects on the spectral reflectance due to nanophase inclusions in the thin rim layer on the regolith grains. We have shown that with realistic grain and inclusion sizes (10 μm and 20 nm, respectively) and with the best available refractive index models, we can reproduce very realistic space-weathering effects on olivine. The *in silico* simulated behavior nicely follows the laboratory experiments in, e.g., Sasaki et al. (2002), Brunetto et al. (2006), Kohout et al. (2014).

Our simulation method relies on the accurate treatment of the small-scale inclusions and on the geometric-optics treatment of the regolith grains. Only the principal physical properties of the materials, i.e., size, volume density, refractive index, are needed as input. Our method offers a versatile tool to study space-weathering effects. We foresee that our model can be used in predicting the effect of different sizes and fractions of nanoinclusions, as well as predicting space-weathering effects due to other materials than nanophase iron, such as iron sulfide or carbon. In addition, we propose that this model can be used in inverse problems, for example in inverting the fraction of the space-weathering products in the material, which could be linked to the time of exposure to the solar radiation, and therefore to the age of the surface, or in deconvoluting the non-weathered material spectra from the observed spectra.

Finally, we report no evidence of the UV reflectance increase with the npFe^0 and olivine materials. We show that the spectral slope changes with the so-called UV bluing effect are produced by the rapid

reflectance decrease at the visual wavelengths close to 550 nm, and not by effects at UV wavelengths. Therefore, if observing olivine-rich targets such as the A/S/Q-type asteroids, the space-weathering effects are seen much more prominently close to 550 nm than at UV wavelengths, where the reflectance of both the fresh and the weathered mineral is very low.

We conclude that if increased (absolute, not the apparent increase when normalized) UV reflectance is seen with iron-rich olivine materials, it is most probably caused by other effects than the npFe^0. For example, the particle size effects discussed by Brown (2014) would fit better with the larger Britt–Pieters inclusions, or with the erosion of the olivine grains themselves by space weathering so that there would be a pronounced fraction of small particles of about 100 nm in the regolith surface (Brown, 2014b). Finally, with carbon-rich materials such as the C/B-type asteroids, the role of the space-weathering products in the spectral changes need to be studied further using complex refractive index models for carbon and other relevant compounds in these bodies. Our multi-scale simulation method offers a suitable approach for these studies.

Acknowledgments

References

Brown, A., 2014a. Equivalence relations and symmetries for laboratory, LIDAR, and planetary Müeller matrix scattering geometries. J. Opt. Soc. Amer. A 31 (12), 2789–2794. http://dx.doi.org/10.1364/JOSAA.31.002789.

Brown, A., 2014b. Spectral bluing induced by small particles under the Mie and Rayleigh regimes. Icarus 239, 85–95. http://dx.doi.org/10.1016/j.icarus.2014.05.042.

Brunetto, R., Romano, F., Blanco, A., Fonti, S., Martino, M., Orofino, V., Verrienti, C., 2006. Space weathering of silicates simulated by nanosecond pulse UV excimer laser. Icarus 180 (2), 546–554. http://dx.doi.org/10.1016/j.icarus.2005.10.016.

Cahill, J., Blewett, D., Nguyen, V., Boosalis, A., Lawrence, S., Denevi, B., 2019. Optical constants of iron and nickel metal and an assessment of their relative influences on silicate mixture spectra from the FUV to the NIR. Icarus 317, 229–241. http://dx.doi.org/10.1016/j.icarus.2018.07.008.

Chapman, C., 2004. Space weathering of asteroid surfaces. Annu. Rev. Earth Planet. Sci. 32 (1), 539–567. http://dx.doi.org/10.1146/annurev.earth.32.101802.120453.

Deb, D., 2015. On the size distribution functions and their application in regolith studies. Adv. Space Res. 55 (1), 477–490. http://dx.doi.org/10.1016/j.asr.2014.09.021.

Escobar-Cerezo, J., Penttilä, A., Kohout, T., Muñoz, O., Moreno, F., Muinonen, K., 2018. Simulations of effects of nanophase iron space weather products on Lunar regolith reflectance spectra. Agron. J. 853 (1), 71. http://dx.doi.org/10.3847/1538-4357/aaa24d.

Gillis-Davis, J., Lucey, P., Bradley, J., Ishii, H., Kaluna, H., Misra, A., Connolly, H., 2017. Incremental laser space weathering of Allende reveals non-lunar like space weathering effects. Icarus 286, 1–14. http://dx.doi.org/10.1016/j.icarus.2016.12.031.

Hapke, B., 2001. Space weathering from mercury to the asteroid belt. J. Geophys. Res. 106 (E5), 10039–10073. http://dx.doi.org/10.1029/2000JE001338.

Hendrix, A., Vilas, F., 2006. The effects of space weathering at UV wavelengths: S-class asteroids. Astron. J. 132 (3), 1396–1404. http://dx.doi.org/10.1086/506426.

Jiang, T., Zhang, H., Yang, Y., Hu, X., Ma, P., Sun, Y., Britt, D., Wang, W., Lu, X., Huang, J., Hsu, W., Mei, B., Wei, R., 2019. Bi-directional reflectance and polarization measurements of pulse-laser irradiated airless body analog materials. Icarus 331, 127–147. http://dx.doi.org/10.1016/j.icarus.2019.05.022.

Keller, L., McKay, D., 1997. The nature and origin of rims on lunar soil grains. Geochim. Cosmochim. Acta 61 (11), 2331–2341. http://dx.doi.org/10.1016/S0016-7037(97)00085-9.

Kohout, T., Čuda, J., Filip, J., Britt, D., Bradley, T., Tuček, J., Skála, R., Kletetschka, G., Kašlík, J., Malina, O., Šišková, K., Zbořil, R., 2014. Space weathering simulations through controlled growth of iron nanoparticles on olivine. Icarus 237 (15), 75–83. http://dx.doi.org/10.1016/j.icarus.2014.04.004.

Lindqvist, H., Martikainen, J., Räbinä, J., Penttilä, A., Muinonen, K., 2018. Ray optics in absorbing media with application to ice crystals at near-infrared wavelengths. J. Quant. Spectrosc. Radiat. Transfer 217, 329–337. http://dx.doi.org/10.1016/j.jqsrt.2018.06.005.

Liu, T., Pang, Y., Zhu, M., Kobayashi, S., 2014. Microporous Co@CoO nanoparticles with superior microwave absorption properties. Nanoscale 6, 2447–2454. http://dx.doi.org/10.1039/C3NR05238A.

Lucey, P., Riner, M., 2011. The optical effects of small iron particles that darken but do not redden: Evidence of intense space weathering on mercury. Icarus 212 (2), 451–462. http://dx.doi.org/10.1016/j.icarus.2011.01.022.

Markkanen, J., Väisänen, T., Penttilä, A., Muinonen, K., 2018. Scattering and absorption in dense discrete random media of irregular particles. Opt. Lett. 43 (12), 2925–2928. http://dx.doi.org/10.1364/OL.43.002925.

Martikainen, J., Penttilä, A., Gritsevich, M., Lindqvist, H., Muinonen, K., 2018. Spectral modeling of meteorites at UV-Vis-NIR wavelengths. J. Quant. Spectrosc. Radiat. Transfer 204, 144–151. http://dx.doi.org/10.1016/j.jqsrt.2017.09.017.

Matsuoka, M., Nakamura, T., Kimura, Y., Hiroi, T., Nakamura, R., Okumura, S., Sasaki, S., 2015. Pulse-laser irradiation experiments of Murchison CM2 chondrite for reproducing space weathering on C-type asteroids. Icarus 254, 135–143. http://dx.doi.org/10.1016/j.icarus.2015.02.029.

Mishchenko, M., Hovenier, J., Travis, L. (Eds.), 2000. Light Scattering by Nonspherical Particles: Theory, Measurements, and Applications. Academic Press.

Moroz, L., Starukhina, L., Snata Rout, S., Sasaki, S., Helbert, J., Baither, D., Bischoff, A., Hiesinger, H., 2014. Space weathering of silicate regoliths with various FeO contents: New insights from laser irradiation experiments and theoretical spectral simulations. Icarus 235, 187–206. http://dx.doi.org/10.1016/j.icarus.2014.03.021.

Muinonen, K., 2004. Coherent backscattering of light by complex random media of spherical scatterers: numerical solution. Waves Random Media 14, 365–388.

Muinonen, K., Markkanen, J., Väisänen, T., Peltoniemi, J., Penttilä, A., 2018. Multiple scattering of light in discrete random media using incoherent interactions. Opt. Lett. 43 (4), 683–686. http://dx.doi.org/10.1364/OL.43.000683.

Muinonen, K., Nousiainen, T., Fast, P., Lumme, K., Peltoniemi, J., 1996. Light scattering by Gaussian random particles: Ray optics approximation. J. Quant. Spectrosc. Radiat. Transfer 55 (5), 577–601. http://dx.doi.org/10.1016/0022-4073(96)00003-9.

Muinonen, K., Nousiainen, T., Lindqvist, H., Muñoz, O., Videen, G., 2009. Light scattering by Gaussian particles with internal inclusions and roughened surfaces using ray optics. J. Quant. Spectrosc. Radiat. Transfer 110, 1628–1639.

Noble, S., Keller, L., Pieters, C., 2005. Evidence of space weathering in regolith breccias I: Lunar regolith breccias. Meteorit. Planet. Sci. 40 (3), 397–408. http://dx.doi.org/10.1111/j.1945-5100.2005.tb00390.x.

Noble, S., Pieters, C., 2003. Space weathering on Mercury: Implications for remote sensing. Sol. Syst. Res. 37 (1), 31–35. http://dx.doi.org/10.1023/A:1022395605024.

Noble, S., Pieters, C., Keller, L., 2007. An experimental approach to understanding the optical effects of space weathering. Icarus 192 (2), 629–642. http://dx.doi.org/10.1016/j.icarus.2007.07.021.

Noguchi, T., Nakamura, T., Kimura, M., Zolensky, M., Tanaka, M., Hashimoto, T., Konno, M., Nakato, A., Ogami, T., Fujimura, A., Abe, M., Yada, T., Mukai, T., Ueno, M., Okada, T., Shirai, K., Ishibashi, Y., Okazaki, R., 2011. Incipient space weathering observed on the surface of Itokawa dust particles. Science 333 (6046), 1121–1125. http://dx.doi.org/10.1126/science.1207794.

Penttilä, A., Martikainen, J., Gritsevich, M., Muinonen, K., 2018. Laboratory spectroscopy of meteorite samples at UV-vis-NIR wavelengths: Analysis and discrimination by principal components analysis. J. Quant. Spectrosc. Radiat. Transfer 206, 189–197. http://dx.doi.org/10.1016/j.jqsrt.2017.11.011.

Pieters, C., Noble, S., 2016. Space weathering on airless bodies. J. Geophys. Res.: Planets 121 (10), 1865–1884. http://dx.doi.org/10.1002/2016JE005128.

Sasaki, S., Hiroi, T., Nakamura, K., Hamabe, Y., Kurahashi, E., Yamada, M., 2002. Simulation of space weathering by nanosecond pulse laser heating: dependence on mineral composition, weathering trend of asteroids and discovery of nanophase iron particles. Adv. Space Res. 29 (5), 783–788. http://dx.doi.org/10.1016/S0273-1177(02)00012-1.

Sasaki, S., Kurahashi, E., Yamanaka, C., Nakamura, K., 2003. Laboratory simulation of space weathering: Changes of optical properties and TEM/esr confirmation of nanophase metallic iron. Adv. Space Res. 31 (12), 2537–2542. http://dx.doi.org/10.1016/S0273-1177(03)00575-1.

Väisänen, T., Markkanen, J., Penttilä, A., Muinonen, K., 2019. Radiative transfer with reciprocal transactions: Numerical method and its implementation. PLoS One 14 (1), 1–24. http://dx.doi.org/10.1371/journal.pone.0210155.

van de Hulst, H., 1957. Light scattering by small particles. Wiley, New York.

Vilas, F., Hendrix, A., 2015. The UV/blue effects of space weathering manifested in S-complex asteroids. I. Quantifying change with asteroid age. Astron. J. 150 (2), 64. http://dx.doi.org/10.1088/0004-6256/150/2/64.

Vilas, F., Hendrix, A., Jensen, E., 2015. The UV/blue effects of space weathering manifested in S-complex asteroids II: Probing for less-weathered objects in the solar System. Planet. Space Sci. 118, 273–276. http://dx.doi.org/10.1016/j.pss.2015.06.023.